Atmos. Meas. Tech. Discuss., 5, 7535–7565, 2012
www.atmos-meas-tech-discuss.net/5/7535/2012/
doi:10.5194/amtd-5-7535-2012

Atmospheric Measurement Techniques Discussions

Zernike polynomials applied to apparent solar disk flattening for pressure profile retrievals

E. Dekemper, F. Vanhellemont, N. Mateshvili, G. Franssens, D. Pieroux, C. Bingen, C. Robert, and D. Fussen

Belgian Institute for Space Aeronomy, 3 avenue Circulaire, 1180 Brussels, Belgium

Received: 13 August 2012 – Accepted: 27 September 2012 – Published: 16 October 2012

Correspondence to: E. Dekemper (emmanuel.dekemper@aeronomie.be)

Published by Copernicus Publications on behalf of the European Geosciences Union.

Abstract

We present a passive method for the retrieval of atmospheric pressure profiles based on the measurement of the apparent flattening of the solar disk as observed through the atmosphere by a spaceborne imager. It involves accurate simulations of the solar occultation and uses the Zernike moments to quantify the flattening. This method is expected to achieve retrievals up to the lower mesosphere with uncertainties 10 to 1000 times smaller than the natural variability.

1 Introduction

The measurement of refraction angles was one of the first remote sensing techniques in the field of spaceborne atmospheric science experiments. From the first radio occultation experiment during the Mariner IV mission that ~~allowed to~~ successfully retrieve pressure and temperature information in Mars' atmosphere (Nicks, 1967) to the pictures of the Sun as seen through the Earth's atmosphere by SOFIE (Solar Occultation For Ice Experiment, Gordley et al., 2009a) onboard AIM (Aeronomy of Ice in the Mesosphere), this technique has proved to be a valuable alternative solution with respect to other remote passive methods like the detection of CO_2 or O_2 thermal emissions.

Gordley et al. (2009b) have shown that one can achieve temperature retrievals with an accuracy of ±5 K up to 60 km provided that high spatial sampling of the solar disk is available. Their method is based on accurate Solar upper and lower edge detection during sunset or sunrise in order to measure refraction angles and to retrieve temperature profiles. In this paper, we follow a different strategy: by taking advantage of the asymmetrical flattening of the apparent solar disk caused by the gradient in the air density profile, we ~~study the possibility to~~ retrieve atmospheric pressure from a quantified description of the whole solar disk deformation. For this purpose, we used Zernike polynomials to guarantee a unique orthogonal decomposition of the images. By simulating

AMTD
5, 7535–7565, 2012

a wide variety of test cases, we managed to build a look up table to map the link between the Zernike moments of the images and the pressure state of the atmosphere.

This theoretical study is intended to show the capabilities of a simple technique based on Sun image analysis that could be applied to any solar imager performing occultations. It does not require highly efficient pointing stabilization, and it has the advantage of using all the pixels constituting the solar disk image, allowing for measurements with very high signal-to-noise ratios.

In the following sections, we first describe the steps leading to the simulation of solar images including the solar limb darkening and the apparent solar disk flattening. Then we present the Zernike polynomials and we apply them to simulated sunset pictures for a comprehensive and non-redundant set of atmospheric pressure states, generated by a principal component analysis performed on a representative pressure dataset. Finally, we show that atmospheric pressure profiles from ten randomly generated sunsets can be retrieved and an error budget analysis is performed.

2 Sun image simulation

2.1 Virtual instrument definition

The goal of this study is to exploit the relation between Sun images and atmospheric pressure profiles. To do so, we developed a virtual but realistic imaging instrument whose essential characteristics match those of ACE, the Atmospheric Chemistry Experiment on-board SCISAT-1 (see Bernath et al., 2005; McElroy et al., 2007, for more details) which possesses two imagers that are used for a twofold purpose (Gilbert et al., 2007). They serve primarily as a pointing support to the payload by keeping the full Sun in their field of view. Secondly, as they observe solar occultations through the Earth's atmosphere, they provide information about the spectral transmittance related to the atmospheric extinction profiles in two different spectral regions. The filters central wavelengths are identical to two of the seven channels of the SAGE II instrument

AMTD
5, 7535–7565, 2012

(Mauldin et al., 1985): a visible channel at 525 nm weakly sensitive to aerosols and ozone, and a near infrared (NIR) channel at 1020 nm sensitive to aerosols as well.

The second channel was selected as the reference for our simulations in order to minimize the effect of trace gas absorption (mainly NO_2 and O_3) on the transmitted irradiance in case of actual application of the method to real data. For the sake of realism, we also kept ACE's pixel size and field of view: the image is sampled by an array of 128 × 128 squared pixels dividing a total field of view of 30 mrad, which is about three times larger than the full Sun apparent angular size. Finally, we also preserved ACE's orbital parameters, and placed our virtual sensor on a 650 km circular orbit. By choosing the wavelength, the field of view and the orbit altitude, all the parameters required to simulate Sun images are defined.

2.2 Solar limb darkening

The Sun image simulation requires a description of the solar limb darkening, i.e. the apparent radial decrease of intensity across the solar disk. This darkening is also wavelength dependent and has been empirically parameterized by Neckel (2005). Defining $\mu = \cos\beta$ where β is the angle of emission of a Sun ray with respect to the local vertical at the Sun surface, the ratio between the light intensity emitted at this angle $I(\mu)$ and the intensity of rays emitted with $\beta = 0$ (i.e. from the center of the apparent disk) can be fitted by a 5th-order polynomial

$$\frac{I(\mu,\lambda)}{I(\mu=1,\lambda)} = \sum_{i=0}^{5} A_i(\lambda)\mu^i, \quad (1)$$

where the A_i coefficients are functions of the wavelength λ. Keeping the notation of Neckel, the six coefficients are defined by the following relations, where the values of the a_{ij} are given in Table 1:

AMTD
5, 7535–7565, 2012

$$A_0 = a_{00} + a_{01}\lambda^{-1}$$
$$A_1 = a_{10} + a_{11}\lambda^{-1} + a_{15}\lambda^{-5}$$
$$A_2 = a_{20} + a_{25}\lambda^{-5}$$
$$A_3 = a_{30} + a_{35}\lambda^{-5}$$
$$A_4 = a_{40} + a_{45}\lambda^{-5}$$
$$A_5 = a_{50} + a_{55}\lambda^{-5}$$

2.3 Atmospheric refractive index

Atmospheric refraction is the key physical process involved in the apparent flattening of the solar disk when observed through Earth atmosphere. The solar rays that penetrate the Earth's atmosphere experience an air concentration gradient giving rise to refraction. This process depends on the refractive index n of each particular layer. In this study, we assumed hydrostatic equilibrium, making n dependent on pressure (P) and temperature (T). CO_2 and water vapor were also considered according to the Ciddor formula (Ciddor, 1996) which is recommended by the International Association of Geodesy (IAG) for refractive index calculations in the visible and near infrared range in air.

In our model, the P, T and H_2O profiles are based on the US Standard 1976 atmosphere. Only CO_2 has been changed to a more up to date value of 400 ppmv. The division of the atmosphere into layers also follows the US Standard atmosphere: the layers are 1 km thick below 25 km, 2.5 km thick between 25 km and 50 km, and 5 km thick from 50 km to 100 km. A spline interpolation was performed to avoid discontinuities over multiple layers.

AMTD
5, 7535–7565, 2012

2.4 1-D ray tracing problem

The problem of simulating solar pictures as acquired after propagation of the light in the atmosphere mostly relies on the knowledge of three parameters: there is only one path for light rays leaving the solar photosphere with a given emission angle β to graze the Earth's surface at a minimal tangent height h and hit the detector with a given viewing angle θ. The geometry is illustrated in Fig. 1 (left panel) for rays lying in the plane containing the centers of the Sun, the Earth and the spacecraft. The formalism used in the present section and the next one is an adapted version of a previous study from Vokrouhlicky et al. (1993).

The trajectory of a light ray in a refractive medium is governed by Fermat's principle, stating that light always follows the fastest path. The associated distance L traveled between time t_A and time t_B is

$$L = \int_{s(t_A)}^{s(t_B)} n(s)\mathrm{d}s,$$

where $n(s)$ is the refractive index at the coordinate s along the path. Furthermore, assuming spherical homogeneous atmospheric layers, the following conservation formula holds for any value of s:

$$n(r(s)) \cdot r(s) \cdot \sin\psi(s) = c^{\mathrm{st}} \quad (2)$$

where c^{st} is a constant value, r denotes the geocentric distance of a point located at a coordinate s along the trajectory, and ψ is the angle between the local vertical and the ray trajectory. Applying Eq. (2) to the point of the light trajectory situated at the smallest distance from the ground, at the altitude h, one can find the relation between the tangent height h and the viewing angle θ (angle between the light ray hitting the detector and the geocentric position vector of the spacecraft):

$$n(h(\theta)) \cdot (R_{\mathrm{E}} + h(\theta)) = d_{\mathrm{ES}} \cdot \sin\theta \quad (3)$$

AMTD
5, 7535–7565, 2012

where R_E is the Earth radius and d_{ES} the geocentric spacecraft distance.

In order to find the relation between the viewing angle θ, the tangent height h and the emission angle β, one can apply some trigonometric relations to the triangles of Fig. 1:

$$\beta(\theta) = \alpha - \xi(\theta), \tag{4}$$

where

$$\xi(\theta) = \pi + 2\delta(h(\theta)) - \omega - \theta, \tag{5}$$

2δ being the total refraction angle, ω, the Sun-Earth-Satellite angle, and α, the angle between the Sun geocentric position vector and the heliocentric position vector of the emission spot. The refraction angle 2δ depends on all the atmospheric layers crossed by the light ray, from the top of the atmosphere (TOA) to the lowest altitude, i.e. the tangent height. The tangent height-dependent refraction angle can be obtained by using the following expression (see for instance Dalaudier et al., 2001, for more details on the computation of refraction angles in the atmosphere):

$$2\delta(h) = -\int_{R_E+h}^{\infty} \frac{2n(h)\cdot(R_E+h)}{n(r)\cdot\sqrt{(n(r)\cdot r)^2 - (n(h)\cdot(R_E+h))^2}} \left(\frac{dn}{dr}\right) dr \tag{6}$$

The last step to solve Eq. (4) with respect to θ is to remove the dependence on α by applying trigonometric relations, leading to the emission angle associated to a light ray having reached the tangent height h and being seen by the instrument at the angle θ (more details can be found in Vokrouhlicky et al., 1993):

$$\beta(\theta) = \left| \sin^{-1}\left(\frac{1}{\rho_1}(\rho_2 \sin\theta - \sin\xi(\theta))\right)\right| \tag{7}$$

where $\rho_1 = R_S/d_{SE}$ with R_S being the solar radius and d_{SE} being the Sun-Earth distance, and $\rho_2 = d_{ES}/d_{SE}$.

AMTD
5, 7535–7565, 2012

2.5 2-D ray tracing problem

Up to now, only emission points lying in the Sun-Earth-spacecraft plane (SES plane) have been considered, as illustrated by the left panel of Fig. 1. It was possible to address them with a single viewing angle (θ). For points located outside the SES plane, one can split their associated viewing angle into the vertical viewing angle θ and a horizontal viewing angle ϕ, allowing to univocally associate the image pixels with the couple of coordinates (ϕ, θ). The origin of the frame is chosen such that $(0,0)$ points towards the Earth center and the θ-axis belongs to the SES plane. The solar disk center receives coordinates $(0, \theta_c)$. This is illustrated in the right panel of Fig. 1.

When no refraction occurs along the light path, the solar limb darkening is a radial effect only, i.e. the emission angle β of the detected photons is the same for points located at an equal distance of the solar disk center ($\phi^2 + (\theta - \theta_c)^2 = c^{ste}$), allowing for a 1-dimensional treatment. But when observed through an inhomogeneous refractive medium, the radial symmetry does not hold anymore and the relation between the light ray emission angle and the viewing angle has to be computed for any combination of θ and ϕ.

Equation (7) relates β to θ in the SES plane, whose intersection with the Sun forms a disk. It allows to compute the limb darkening along the vertical direction for this particular meridian. We will first extend the validity of Eq. (7) to the other adjacent slices of the Sun, then correct it for the limb darkening along the horizontal direction (which does not suffer from any atmospheric effect as no horizontal atmospheric gradient is considered).

This is more easily done by dividing the Sun into vertical slices of infinitesimal width. Every point belonging to the surface of a given slice is seen with the same ϕ angle and each slice is actually a disk whose radius $R_S(\phi)$ is approximately computed by the following relation:

$$R_S(\phi) \approx \sqrt{R_S^2 - (d_{SE} \cdot \phi)^2}. \quad (8)$$

AMTD
5, 7535–7565, 2012

Obviously, $R_S(\phi)$ decreases with ϕ and vanishes when ϕ is equal to half of the angular size of the Sun.

The limb darkening caused by a non-zero β angle within a ϕ-slice is obtained by using $R_S(\phi)$ instead of R_S in the calculation of ρ_1 in Eq. (7). One obtains an updated expression for β taking into account the reduction of the vertical angular size of the ϕ-slices:

$$\beta(\phi,\theta) = \left| \sin^{-1}\left(\frac{1}{\rho_1(\phi)} (\rho_2 \sin\theta - \sin\xi(\theta)) \right) \right| . \quad (9)$$

There remains to update the parameter μ involved in Eq. (1) with respect to $\beta(\phi,\theta)$, and account for the limb darkening along the horizontal direction:

$$\mu(\phi,\theta) = \cos\left(\sqrt{\beta^2(\phi,\theta) + \arcsin^2\left(\frac{d_{SE}\cdot\phi}{R_S} \right)} \right) \quad (10)$$

To illustrate the effect of the atmospheric refraction on the apparent solar disk, we simulated images of the Sun for different Sun-Earth-spacecraft arguments ω. Two of them are shown in Fig. 2. When ω increases during the occultation, the light ray bending increases also due to higher air density resulting in an asymmetrical flattening of the Sun image as light rays from the lower part of the Sun are more bent than those from the higher part.

The Sun images were computed according to the following procedure:

– For a given state of the atmosphere (pressure, temperature, humidity, ...) the total refraction angle $2\delta(h)$ is computed for all tangent altitudes using Eq. (6) (the computation grid size is 10 m, with interpolation of the geophysical quantities on this finer grid).

AMTD
5, 7535–7565, 2012

– The emission angle β and the limb darkening parameter μ are computed on a fine grid of regularly spaced values of (ϕ, θ). Equation (3) is solved iteratively to match θ with h using the pre-computed $2\delta(h)$.

– Each virtual pixel intensity is computed by integrating $I(\mu(\phi,\theta), 1020\,\text{nm})$ over its field of view.

3 Zernike moments

As the goal of this work is to retrieve atmospheric pressure information from the apparent flattening of the solar disk, a unique quantitative description of the Sun shape is preferable. It is also necessary to have a method insensitive to spacecraft pointing uncertainties responsible for rotation and translation of the Sun in the FOV. For these reasons, we selected the Zernike polynomials.

Zernike polynomials (Zernike, 1934) constitute an orthogonal basis of continuous functions defined on the unit disk. They are widely used in adaptive optics to correct for image deformation due to atmospheric effects in high precision telescopes for instance. The definition of the Zernike polynomial of order n and repetition m (n and m being always integers with $n \geq 0$ and $|m| \leq n$ with $n - |m|$ even) in polar coordinates (ρ, α) is

$$Z_n^m(\rho,\alpha) = R_n^m(\rho) \cdot e^{im\alpha}. \tag{11}$$

The radial function is given by the following polynomial:

$$R_n^m(\rho,\alpha) = \sum_{s=0}^{(n-|m|)/2} \frac{(-1)^s (n-s)!}{s!\left(\frac{n+|m|}{2}-s\right)!\left(\frac{n-|m|}{2}-s\right)!} \rho^{n-2s}. \tag{12}$$

One immediately notices that $Z_n^{m^*} = Z_n^{-m}$. Figure 3 shows the Zernike polynomials computed on the unit disk up to $n = 4$.

AMTD
5, 7535–7565, 2012

For our application, Cartesian coordinates are preferably used than polar ones, i.e. $Z_n^m(\rho,\alpha)$ is equivalent to $Z_n^m(x,y)$ with $x^2+y^2 \leq 1$. By orthogonality of the Zernike functions, we have

$$\iint_{x^2+y^2\leq 1} Z_n^{m^*}(x,y) Z_j^k(x,y) \mathrm{d}x\mathrm{d}y = \frac{\pi}{n+1}\delta_{nj}\delta_{mk}. \quad (13)$$

When applying Zernike polynomials to images, one needs to discretize the functions to account for the discrete nature of digital pictures. This may lead to a loss of orthogonality. This problem was already discussed by Wang and Silva (1980) but an extensive study of the orthogonality requirement of the discrete Zernike polynomials has been performed by Allen (2010) where different grid geometries (Cartesian, polar, random, ...) and grid resolutions (number of grid nodes) were tested. The goal was to find the best discretization strategy, close to the perfect orthogonality of the continuous case. Allen showed, as expected, that a finer grid allows for better orthogonality. In the case of a Cartesian grid like in digital images, a rule of thumb for estimating the minimal number of grid points n_p ensuring "decent orthogonality" between the n_z first Zernike polynomials is to satisfy $\log_{10} n_\mathrm{p} > 1.73 \log_{10} n_\mathrm{z} + 0.27$. According to this rule, for applications where the 10 first Zernike polynomials are needed, the picture should be made of 100 pixels at least. In our case, images are cropped such that they closely fit the left and right edges of the solar disk, which makes the final array 45×45 pixels large. Not all of them belong to the unit circle, the pixels close to the corners are excluded from the Zernike domain, which leaves us with a bit more than 1500 pixels concerned. As will be shown later, we will not use many Zernike polynomials, so that the uniqueness of the decomposition will be guaranteed.

The moment of order n and repetition m of the image whose pixels intensities are represented by $f(x,y)$ is given by the following expression:

$$A_n^m = \frac{n+1}{\pi} \sum_x \sum_y f(x,y) \cdot Z_n^{m^*}(x,y), \qquad x^2+y^2 \leq 1. \quad (14)$$

AMTD
5, 7535–7565, 2012

There is no guarantee that the solar disk will always remain exactly at the same position in the field of view. It can be shown that Zernike moments are invariant under translation and rotation (Khotanzad and Hong, 1990): the Zernike moment A_n^m of a given image becomes $A_n^{m^r}$ after a rotation by an angle ϵ, and clearly

$$A_n^{m^r} = A_n^m \cdot e^{-im\epsilon},$$

meaning that the moment modulus is preserved under rotation. A consequence of this property is that, as $|A_n^m| = |A_n^{-m}|$, it is sufficient to rely on moments with $m \geq 0$ only.

The translation invariance can be achieved by pre-processing the Sun image in order to have the centroid of the solar disk co-located with the center of the unit disk. It can be done by using the regular moments (Hu, 1962). In their discrete form, they are defined by the following expression:

$$m_{pq} = \sum_x \sum_y x^p y^q f(x,y). \tag{15}$$

In the Cartesian frame of the initial image, the centroid is located at $(\overline{x}, \overline{y})$ where

$$\overline{x} = \frac{m_{10}}{m_{00}}, \qquad \overline{y} = \frac{m_{01}}{m_{00}}.$$

In the translated coordinates frame (x', y'), the image is centered in such a way that $f(x', y') = f(x - \overline{x}, y - \overline{y})$.

It can be shown (Khotanzad and Hong, 1990) that Zernike moments of order $n = 1$, being A_1^{-1} and A_1^1, are proportional to the regular moments m_{10} and m_{01}. Both of them vanish in the translated frame, resulting in the disappearance of the first order Zernike moments as well.

In Fig. 4, Zernike moments up to order 4 are computed for the high and low Sun cases. The first moment A_0^0 is by definition the total integrated intensity on the whole solar disk and is always dominant.

AMTD
5, 7535–7565, 2012

4 Test case: pressure profiles retrieval

The problem investigated in this work can be summarized in this way: how to retrieve pressure profiles from Sun images? The measurements do not consist of the images themselves, but on a number of Zernike moments $A_n^m(\omega)$ computed for each image $I(\omega)$ acquired successively during sunset or sunrise, ω being the Sun-Earth-Spacecraft argument. From a given set of Zernike moments, the measurement vector $\boldsymbol{a}$ is written as:

$$\boldsymbol{a} = \begin{pmatrix} \boldsymbol{A}(\omega_1) \\ \vdots \\ \boldsymbol{A}(\omega_s) \end{pmatrix} \quad \text{with} \quad \boldsymbol{A}(\omega_i) = \begin{pmatrix} A_{n_1}^{m_1}(\omega_i) \\ \vdots \\ A_{n_k}^{m_k}(\omega_i) \end{pmatrix}, \tag{16}$$

$A_{n_j}^{m_j}(\omega_i)$ being the j-th selected moment computed on the i-th image. The atmospheric pressure profile will be referred as the state vector $\boldsymbol{p}$, made of 46 layers of constant pressure (US Standard atmosphere). The forward model can be simply written as:

$$\boldsymbol{a} = F(\boldsymbol{p}) \tag{17}$$

where F describes the ray propagation, the image acquisition and the moments computation.

Equation (17) is not solved straightforward due to the non-linearity of operator F through the refraction process itself. Ill-conditioning might also be an issue: even if the number of image acquisitions is larger than the number of retrieved parameters, the problem might be ill-conditioned due to the redundancy between successive measurements. Furthermore, iterative approaches are not suitable as all the pictures of the setting or rising Sun need to be simulated at each iteration, which is not efficient regarding the processing time. To circumvent this difficulty, we preferred a retrieval strategy based on a lookup table. By simulating sunsets for a large number of plausible pressure profiles, we built a large set of direct relations between pressure profiles and

AMTD
5, 7535–7565, 2012

associated Zernike moments. The pressure profiles used to create the lookup table constitute the training dataset. If the training dataset is sufficiently exhaustive with respect to the natural variation of atmospheric pressure, then any pressure profile should be well captured by the lookup table.

The first step is to have a clear representation of the variety of realistic pressure states. We used the COSPAR International Reference Atmosphere model (Rees et al., 1990) referred in the following as CIRA-86. It consists of monthly averaged zonal pressure data on an altitude grid spacing of 5 km from 20 km to 120 km between −80° and 80° of latitude by steps of 10°, forming a dataset of 204 profiles. To comply with the US Standard atmosphere, the pressure profiles were extrapolated down to 0 km by setting a common value of 101 300 Pa at ground for all profiles. They were then interpolated onto the US Standard atmosphere grid using a spline method. The dataset consists of a matrix of 204 realizations (the modified CIRA-86 profiles) of 46 variables (the number of atmospheric layers). Let $\boldsymbol{p} = (p_1 \cdots p_q)$ be a pressure vector where $q = 46$ in this case. The whole dataset is represented by the matrix

$$\mathbf{P} = \begin{pmatrix} p_{11} \cdots p_{1q} \\ \vdots \quad\quad \vdots \\ p_{r1} \cdots p_{rq} \end{pmatrix},$$

with p_{ij} being the i-th realization of the j-th variable (i.e. the i-th pressure value of the j-th layer), where $i = 1, \ldots, r$ ($r = 204$ for CIRA-86) and $j = 1, \ldots, q$.

However, the profiles may contain redundant structures between each other and it could be useful to describe the pressure profiles with a reduced number of parameters. We used Empirical Orthogonal Functions (EOF) (Lorenz, 1956), often referred to as Principal Component Analysis (PCA) (Jolliffe, 2002) to solve these issues. The technique is based on finding orthogonal vectors (the principal axes) along the directions in which most of the dispersion of repeated realizations of the same phenomenon occurs. In the following paragraphs, we focus on finding the principal axes explaining most of

AMTD
5, 7535–7565, 2012

the variation of the atmospheric pressure profiles dataset and on estimating the error of such a reduced representation.

The dataset is first centered about its mean. By averaging the realizations of each variable, we define

$$\overline{\mathbf{P}} = \begin{pmatrix} \overline{p_1} \cdots \overline{p_q} \\ \vdots \quad \vdots \\ \overline{p_1} \cdots \overline{p_q} \end{pmatrix} \quad \text{where} \quad \overline{p_j} = \frac{1}{r} \sum_{i=1}^{r} p_{ij}.$$

The centered dataset is denoted by $\tilde{\mathbf{P}} = \mathbf{P} - \overline{\mathbf{P}}$. Then the data are normalized by their standard deviation. The covariance matrix of $\tilde{\mathbf{P}}$ is $\mathbf{\Sigma} = \tilde{\mathbf{P}}^{\mathrm{T}} \cdot \tilde{\mathbf{P}}$ with its elements being the σ_{ij}, $i, j = 1, \ldots, q$, and $\mathbf{\Sigma}_0$ is the same matrix but with all off-diagonal elements removed. The factor $1/(q-1)$ has been neglected. The normalized dataset is then

$$\mathbf{P}^* = \tilde{\mathbf{P}} \cdot \mathbf{\Sigma}_0^{-1/2} \tag{18}$$

whose elements are the $p^*_{ij} = \left(p_{ij} - \overline{p_j}\right) / \sqrt{\sigma_{jj}}$. By performing a singular value decomposition (SVD) on the normalized dataset, the eigenvectors (the principal axes) are identified and their associated singular values are sorted in a decreasing order. Defining the matrices $\mathbf{U}$, $\mathbf{L}$ and $\mathbf{V}$ such that $\mathbf{U}^{\mathrm{T}}\mathbf{U} = \mathbf{V}^{\mathrm{T}}\mathbf{V} = \mathbf{I}$, and $\mathbf{L}$ is diagonal, we have $\mathbf{P}^* = \mathbf{U}\mathbf{L}\mathbf{V}^{\mathrm{T}}$. The covariance matrix of $\mathbf{P}^*$ follows: $\mathbf{R} = \mathbf{P}^{*\mathrm{T}}\mathbf{P}^* = \mathbf{V}\mathbf{L}\mathbf{L}\mathbf{V}^{\mathrm{T}} = \mathbf{V}\mathbf{\Lambda}\mathbf{V}^{\mathrm{T}}$, where the columns of $\mathbf{V}$ are the eigenvectors of $\mathbf{R}$, and the λ_{ij} of the diagonal matrix $\mathbf{\Lambda}$ are its squared singular values. From now on, the columns of $\mathbf{V}$ will be called the principal axes (PA) of the normalized dataset. The principal components (PC) of a given pressure profile are its coordinates in the orthogonal basis formed by the PA. Computing the PCs of the entire normalized dataset, we find the matrix of PCs $\mathbf{C}$ of size $r \times q$:

$$\mathbf{C} = \mathbf{P}^*\mathbf{V}.$$

Exploring the eigenvalues of the SVD, we find that the first ones already explain a very large portion of the overall dataset variability. Table 2 shows the eigenvalues

AMTD
5, 7535–7565, 2012

and their cumulative importance for the 10 first PA. One notices that the first four PA are responsible for more than 99 % of the variance.

As the goal is to reduce the number of dimensions of the pressure profiles, we are looking for the minimum number of PA needed to allow for a reconstruction of the dataset profiles within acceptable errors. The satisfaction criterium is based on the global mean quadratic relative error (MQRE) that we required to be lower than 1 % for the full dataset. The global MQRE is computed this way: from a number of m PA ($1 \leq m \leq q$), the profiles are reconstructed using the associated m PCs:

$$\begin{aligned} & \mathbf{P}^{*}_{(m)} = \mathbf{C}_{(m)}\mathbf{V}^{\mathrm{T}}_{m} \\ \Leftrightarrow & \left(\mathbf{P}_{(m)} - \overline{\mathbf{P}}\right) \cdot \boldsymbol{\Sigma}_{0}^{-1/2} = \mathbf{C}_{(m)}\mathbf{V}^{\mathrm{T}}_{m} \\ \Leftrightarrow & \mathbf{P}_{(m)} = \mathbf{C}_{(m)}\mathbf{V}^{\mathrm{T}}_{m}\boldsymbol{\Sigma}_{0}^{1/2} + \overline{\mathbf{P}} \end{aligned} \tag{19}$$

where $\mathbf{V}_m$ is a $q \times m$ matrix containing the m first PA, and the subscript (m) denotes quantities obtained from the truncated basis of these m first PA. The MQRE ($\overline{\epsilon}$) is computed by averaging the relative deviation between the initial data (p_{ij}) and the reconstructed ones ($p_{ij}^{(m)}$):

$$\overline{\epsilon}_{(m)} = \sqrt{\frac{1}{rq}\sum_{j=1}^{q}\sum_{i=1}^{r}\left(\frac{p_{ij} - p_{ij}^{(m)}}{p_{ij}}\right)^{2}} \cdot 100\,[\%] \tag{20}$$

The last column of Table 2 provides the MQRE computed for up to 10 PA. As can be seen, five PA are needed to go below the 1 % threshold.

When the 204 profiles of the CIRA-86 database are projected onto the five first principal axes, their PCs can be seen as a spectrum. Figure 5 shows the spectrum of PCs for each principal axis. In order to build a training database that would span almost all possible atmospheric states and to avoid redundancies between profiles (as it is

AMTD
5, 7535–7565, 2012

the case in CIRA-86), we used the principal components spectra to identify a small number of pivot values from which an exhaustive but non-redundant dataset can be generated. Table 3 shows the coordinates of the pivots along the five principal axes and how they have been computed. By combining the pivots, one can create a new database of $4^2 \cdot 3^3 = 432$ different pressure profiles that constitutes the training dataset that will be used in the retrieval algorithm.

The measurement simulations consist of 23 pictures of the setting Sun. Each picture corresponds to a given value of ω, the Sun-Earth-Spacecraft argument: from 113.25° (high Sun) up to 115.45° (low Sun) by steps of 0.1°. The images are then projected onto the Zernike polynomials basis and the Zernike moments are computed. Only a small number k of them are kept for the training. If there are l image pixels falling within the circular domain of the Zernike functions, ordered in a column vector $\boldsymbol{f}(\omega_i, \boldsymbol{p}_j)$ (ω_i is the i-th angle during the sunset and $\boldsymbol{p}_j$ is the j-th pressure profile in the dataset), then in matrix formalism, the vector containing the Zernike moments is computed by

$$\boldsymbol{a}_{ij} = \underbrace{\boldsymbol{a}(\omega_i, \boldsymbol{p}_j)}_{k\times 1} = \underbrace{\mathbf{Z}}_{k\times l} \cdot \underbrace{\boldsymbol{f}(\omega_i, \boldsymbol{p}_j)}_{l\times 1}$$

where the rows of $\mathbf{Z}$ are the k selected Zernike polynomials evaluated at the l pixels lying in the circular domain of the image. The Zernike moments of each image and each pressure profile are then concatenated into a matrix $\mathbf{A}$ of size $[23 \cdot k \times 432]$ to form the measurement matrix of the training dataset.

The relation between the measurements of matrix $\mathbf{A}$ and the 5 principal components of the pressure profiles arranged in the matrix $\mathbf{C}$ of size $[5 \times 432]$ is expressed by the transfer matrix $\mathbf{X}$ of size $[5 \times 23 \cdot k]$:

$$\mathbf{C}_{\text{train}} = \mathbf{X} \cdot \mathbf{A}_{\text{train}} \tag{21}$$

Finally, the elements of $\mathbf{X}$ can be easily computed through the resolution of this overconstrained problem using a least-square regression method:

$$\mathbf{X} = \mathbf{C}_{\text{train}} \cdot \mathbf{A}_{\text{train}}^{\mathrm{T}} \cdot \left(\mathbf{A}_{\text{train}} \cdot \mathbf{A}_{\text{train}}^{\mathrm{T}} \right)^{-1} \tag{22}$$

AMTD
5, 7535–7565, 2012

Once **X** has been determined, it should be possible to retrieve every realistic pressure profile by solving Eq. (21) with the k Zernike moments computed from the 23 images of the sunset. Figure 6 shows the relative deviation between ten randomly generated pressure profiles and the retrieved ones by the use of the first Zernike moment only (A_0^0 which corresponds to the total intensity of the solar disk). One can observe that the retrieval is excellent up to 40 km. Above this altitude, the error increases for profiles whose PCs lie closer to the edges of the training data distribution.

By looking at the evolution of the moments A_0^0, A_2^0 and A_2^2, plotted in the three right panels of Fig. 6 it becomes also clear that one cannot expect good results above 60 km as the different profiles show almost no difference in their Zernike moments. In other words, the deformation of the solar disk starts becoming detectable with our detector resolution and at our chosen wavelength only below an apparent altitude of 60 km.

~~If this method had to be applied~~ in real conditions, many sources of errors should be included in the development with a major contribution from shot noise and detector dark current. The error budget can be computed by starting from the covariance matrix of each image: a diagonal matrix $\mathbf{S}_{\boldsymbol{f}_i}$ of size $[l \times l]$ containing the shot noises of each pixel belonging to the circle domain. From there, $\mathbf{S}_{\boldsymbol{f}_i}$, the covariance matrix of $\boldsymbol{a}_i$, of size $[k \times k]$ follows:

$$\mathbf{S}_{a_i} = \mathbf{Z} \cdot \mathbf{S}_{\boldsymbol{f}_i} \cdot \mathbf{Z}^{\mathrm{T}}. \tag{23}$$

The covariance matrix of the measurement vector (the Zernike moments of the 23 images) is formed by concatenating the $\mathbf{S}_{a_i}$ to form a block-diagonal matrix $\mathbf{S}_{\boldsymbol{a}}$. The covariance matrix of the retrieved PCs is then given by:

$$\mathbf{S}_{\mathrm{C}} = \mathbf{X} \cdot \mathbf{S}_{\boldsymbol{a}} \cdot \mathbf{X}^{\mathrm{T}}. \tag{24}$$

Finally, the covariance matrix of the error on the pressure profile is found using the same procedure on Eq. (19):

$$\mathbf{S}_{\mathrm{P}} = \boldsymbol{\Sigma}_0^{1/2} \mathbf{V} \mathbf{S}_{\mathrm{C}} \mathbf{V}^{\mathrm{T}} \boldsymbol{\Sigma}_0^{1/2}. \tag{25}$$

AMTD
5, 7535–7565, 2012

In order to estimate the expected retrieval error, we simulated a test case where the brightest pixel of the solar pictures receives 10 000 counts and suffers from a dark current of 500 counts. Taking into account the associated shot noises, we used the above formula to derive the retrieval error by taking the square root of the diagonal elements of $\mathbf{S}_P$. By examining the relative importance of this error to the profile, we find values ranging typically from 0.001 % for the lower layers, to 10 % for the highest ones. These typical numbers have to be compared with the natural variability of the pressure profiles as can be computed using the CIRA-86 dataset: a few percent at lower altitudes to a hundred percent at the highest ones. This exercise, though very simple, allows to conclude that thanks to the high signal to noise ratio of the measurement vector (the Zernike moments use all the pixels of the solar disk resulting in a huge amount of signal), the retrieval error is expected to be 10 to 1000 times smaller than the natural variability of the retrieved quantity.

5 Discussions and conclusions

This theoretical study was performed in order to show that one could retrieve atmospheric pressure profiles up to the lower mesosphere by means of solar disk image analysis. Its intrinsic advantages are absence of strong pointing requirements (as the Sun is a very intense light source, one only needs to take pictures with sufficiently small integration times to have sharp solar disk images and to keep it in the instrument field of view for the complete sunset/sunrise), high signal to noise ratios (all the pixels sampling the solar disk are used) and potentially applicable to any solar occultation imager dataset provided that the images have been sent to ground in their entirety. The Zernike moments computation could even be performed onboard, requiring the download of a few numbers only (the Zernike moments themselves) instead of the full pixel map intensity. This could be a nice feature for systems having small downlink capacity. s method was actually studied in the frame of the development of ALTIUS (Atmospheric Limb Tracker for the Investigation of the Upcoming Stratosphere), a project of

AMTD
5, 7535–7565, 2012

a new spaceborne instrument aimed at the measurement of atmospheric trace gases using hyperspectral images of the bright limb and solar/stellar occultations.

Finally, as pointed out by Dodion et al. (2007) where the usefulness of imagers for automatic cloud detection is demonstrated, the Zernike moments could be a useful tool for the identification of mesospheric and stratospheric clouds: their presence unavoidably enhance some higher order Zernike moments with respect to the cloud-free images.

This study was performed on the basis of an ACE-imager like instrument. As exhibited by the Zernike moments of Sun pictures at high tangent altitudes, coarse detector grid resolutions do not allow to distinguish small refractive effects. By using smaller pixels, and increasing their number, one can raise the retrieval range by a few more kilometers in the mesosphere: higher order Zernike moments would then allow to resolve pressure variability at the highest layers.

Acknowledgements. We wish to acknowledge the support of the Belgian Science Policy Office (BELSPO) and the ESA-PRODEX programme supporting the ALTIUS project.

References

Allen, J. H.: Orthogonality and Convergence of Discrete Zernike Polynomials, M.Sc. thesis, University of New Mexico, New Mexico, USA, 2010. 7545

Bernath, P. F., McElroy, C. T., Abrams, M. C., Boone, C. D., Butler, M., Camy-Peyret, C., Carleer, M., Clerbaux, C., Coheur, P.-F., Colin, R., DeCola, P., DeMazière, M., Drummond, J. R., Dufour, D., Evans, W. F. J., Fast, H., Fussen, D., Gilbert, K., Jennings, D. E., Llewellyn, E. J., Lowe, R. P., Mahieu, E., McConnell, J. C., McHugh, M., McLeod, S. D., Michaud, R., Midwinter, C., Nassar, R., Nichitiu, F., Nowlan, C., Rinsland, C. P., Rochon, Y. J., Rowlands, N., Semeniuk, K., Simon, P., Skelton, R., Sloan, J. J., Soucy, M.-A., Strong, K., Tremblay, P., Turnbull, D., Walker, K. A., Walkty, I., Wardle, D. A., Wehrle, V., Zander, R., and Zou, J.: Atmospheric Chemistry Experiment (ACE): mission overview, Geophys. Res. Lett., 32, L15S01, doi:10.1029/2005GL022386, 2005. 7537

AMTD
5, 7535–7565, 2012

Ciddor, P. E.: Refractive index of air: new equations for the visible and near infrared, Appl. Optics, 35, 1566–1573, 1996. 7539

Dalaudier, F., Kan, V., and Gurvich, A. S.: Chromatic refraction with global ozone monitoring by occultation of stars. I. Description and scintillation correction, Appl. Optics, 40, 866–877, 2001. 7541

Dodion, J., Fussen, D., Vanhellemont, F., Bingen, C., Mateshvili, N., Gilbert, K., Skelton, R., Turnbull, D., McLeod, S. D., Boone, C. D., Walker, K. A., and Bernath, P. F.: Cloud detection in the upper troposphere-lower stratosphere region via ACE imagers: a qualitative study, J. Geophys. Res., 112, D03208, doi:10.1029/2006JD007160, 2007. 7554

Fussen, D., Vanhellemont, F., and Bingen, C.: Synthesis inverse mapping: a robust method applicable to atmospheric remote sounding, J. Geophys. Res., 107, 4421, doi:10.1029/2002JD002206, 2002.

Gilbert, K. L., Turnbull, D. N., Walker, K. A., Boone, C. D., McLeod, S. D., Butler, M., Skelton, R., Bernath, P. F., Chateauneuf, F., and Soucy, M.-A.: The onboard imagers for the Canadian ACE SCISAT-1 mission, J. Geophys. Res., 112, D12207, doi:10.1029/2006JD007714, 2007. 7537

Gordley, L. L., Hervig, M., Fish, C., Russell III, J. M., Bailey, S., Cook, J., Hansen, S., Shumway, A., Paxton, G., Deaver, L., Marshall, T., Burton, J., Magill, B., Brown, C., Thompson, E., and Kemp, J.: The Solar Occultation For Ice Experiment (SOFIE), J. Atmos. Solar-Terr. Phys., 71, 300–315, doi:10.1016/j.jastp.2008.07.012, 2009a. 7536

Gordley, L. L., Burton, J., Marshall, B. T., McHugh, M., Deaver, L., Nelsen, J., Russell, J. M., and Bailey, S.: High precision refraction measurements by solar imaging during occultation: results from SOFIE, Appl. Optics, 48, 4814–4825, 2009b. 7536

Hu, M. K.: Visual pattern recognition by moment invariants, IRE Trans. Inf. Theory, 8, 179–187, 1962. 7546

Jolliffe, I. T.: Principal Component Analysis, Springer Series in Statistics, Springer, New York, 2002. 7548

Khotanzad, A. and Hong, Y. H.: Invariant image recognition by Zernike moments, IEEE Trans. Pattern Anal., 12, 489–497, 1990. 7546

Lorenz, E. N.: Empirical orthogonal functions and statistical weather prediction, Statistical forecasting project report, Department of Meteorology, Mass. Inst. Tech., Cambridge, Massachusetts, USA, 52 pp., 1956. 7548

AMTD
5, 7535–7565, 2012

Mauldin, L. E., Zaun, N. H., McCormick, M. P., Guy, J. H., and Vaughn, W. R.: Stratospheric aerosol and gas experiment II instrument: a functional description, Opt. Eng., 24, 307–312, 1985. 7538

McElroy, C. T., Nowlan, C. R., Drummond, J. R., Bernath, P. F., Barton, D. V., Dufour, D. G., Midwinter, C., Hall, R. B., Ogyu, A., Ullberg, A., Wardle, D. I., Kar, J., Zou, J., Nichitiu, F., Boone, C. D., Walker, K. A., and Rowlands, N.: The ACE-MAESTRO instrument on SCISAT: description, performance, and preliminary results, Appl. Optics, 46, 4341–4356, 2007. 7537

Neckel, H.: Analytical reference functions $F(\lambda)$ for the Sun's limb darkening and its absolute continuum intensities (300 to 1100 nm), Solar Phys., 229, 13–33, 2005. 7538, 7557

Nicks, O. W.: Review of the Mariner IV results, Moon and Planets, NASA SP-130, Washington DC, 150–185, 1967. 7536

Rees, D., Barnett, J. J., and Labitzke, K.: COSPAR international reference atmosphere: 1986. Part II: middle atmosphere models, Adv. Space Res., 10, Oxford and New-York, 1990. 7548

Teague, M. R.: Image analysis via the general theory of moments, J. Opt. Soc. Am., 70, 920–930, 1980.

Vokrouhlicky, D., Farinella, P., and Mignard, F.: Solar radiation pressure perturbations for Earth satellites. I: A complete theory including penumbra transitions, Astronom. Astrophys., 280, 295–312, 1993. 7540, 7541

Wang, J. Y. and Silva, D. E.: Wave-front interpretation with Zernike polynomials, Appl. Optics, 19, 1510–1518, 1980. 7545

Ward, D. M. and Herman, B. M.: Refractive sounding by use of satellite solar occultation measurements including an assessment of its usefulness to the stratospheric aerosol and gas experiment program, Appl. Optics, 37, 8306–8317, 1998.

Zernike, F.: Beugungstheorie des Schneidenverfahrens und seiner verbesserten Form, der Phasenkontrastmethode, Physica, 1, 689–704, 1934. 7544

AMTD
5, 7535–7565, 2012

Table 1. Values attributed to the limb darkening coefficients as given in Neckel (2005) for wavelengths belonging to the spectral range 422 nm–1100 nm.

a_{00}	=	0.75267	a_{30}	=	2.42234
a_{01}	=	−0.265577	a_{35}	=	−0.017117
a_{10}	=	0.93874	a_{40}	=	−1.71150
a_{11}	=	0.265577	a_{45}	=	0.011977
a_{15}	=	−0.004095	a_{50}	=	0.49062
a_{20}	=	−1.89287	a_{55}	=	−0.003347
a_{25}	=	0.012582			

AMTD
5, 7535–7565, 2012

Table 2. PCA applied to the CIRA-86 pressure dataset. The eigenvalues of the 10 first principal axes and their cumulative importance for capturing the overall dataset variability are given in the first two columns. The third column gives the total relative error made when the dataset is reconstruct by the use of the first PA's only.

	Eigenvalue amplitude	Cumulative importance (%)	MQRE (%)
λ_1	37.1415	82.537	6.08
λ_2	5.7789	95.379	2.85
λ_3	1.5160	98.748	1.95
λ_4	0.3634	99.555	1.29
λ_5	0.1372	99.860	0.66
λ_6	0.0399	99.949	0.42
λ_7	0.0139	99.980	0.26
λ_8	0.0054	99.992	0.17
λ_9	0.0020	99.996	0.13
λ_{10}	0.0011	99.998	0.09

AMTD
5, 7535–7565, 2012

Table 3. Coordinates of the pivots along the five first principal axes. The median $\tilde{m}_i$ and the standard deviation σ_i of each distribution ($i = 1, \ldots, 5$) were used to compute the pivots. They were chosen such as to span the spectrum with a reduced number of points. See Fig. 5 for a representation of the PC spectrum.

	Pivots			
PA#1	$\tilde{m}_1 - 3\sigma_1 = -1.0814$	$\tilde{m}_1 - 1\sigma_1 = -0.2259$	$\tilde{m}_1 = 0.2018$	$\tilde{m}_1 + 1\sigma_1 = 0.6296$
PA#2	$\tilde{m}_2 - 1\sigma_2 = -0.2343$	$\tilde{m}_2 = -0.0656$	$\tilde{m}_2 + 1\sigma_2 = 0.1031$	$\tilde{m}_2 + 3\sigma_2 = 0.4405$
PA#3	$\tilde{m}_3 - 1\sigma_3 = -0.2721$	$\tilde{m}_3 = -0.0128$	$\tilde{m}_3 + 1\sigma_3 = 0.2465$	
PA#4	$\tilde{m}_4 - 1\sigma_4 = -0.1200$	$\tilde{m}_4 = 0.0069$	$\tilde{m}_4 + 1\sigma_4 = 0.1339$	
PA#5	$\tilde{m}_5 - 1\sigma_5 = -0.0756$	$\tilde{m}_5 = 0.0024$	$\tilde{m}_5 + 1\sigma_5 = 0.0804$	

AMTD
5, 7535–7565, 2012

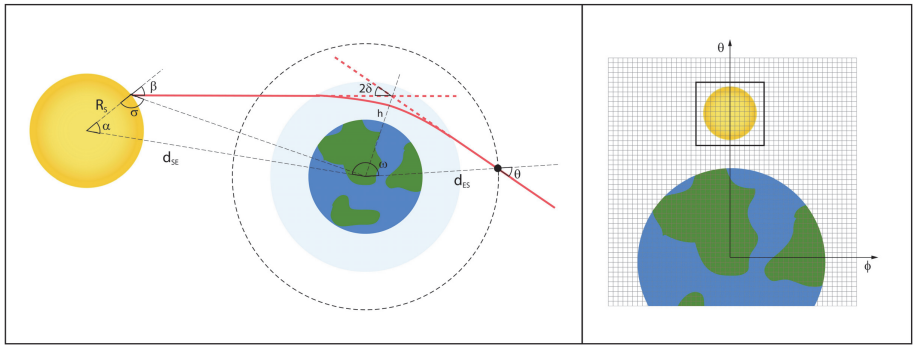

Fig. 1. Left panel: illustration of the 1-dimensional ray tracing problem for photon trajectories in the Sun-Earth-Spacecraft plane. Right panel: illustration of the reference frame for vertical and horizontal viewing directions as seen from the instrument. The origin of the coordinate system is at the intersection of the axes and the black box illustrates a possible instrument field of view. Relative sizes of the Earth, the Sun and the pixels are not representative of the orbit and instrument parameters used in this study.

AMTD
5, 7535–7565, 2012

Zernike polynomials applied to solar disk flattening

E. Dekemper et al.

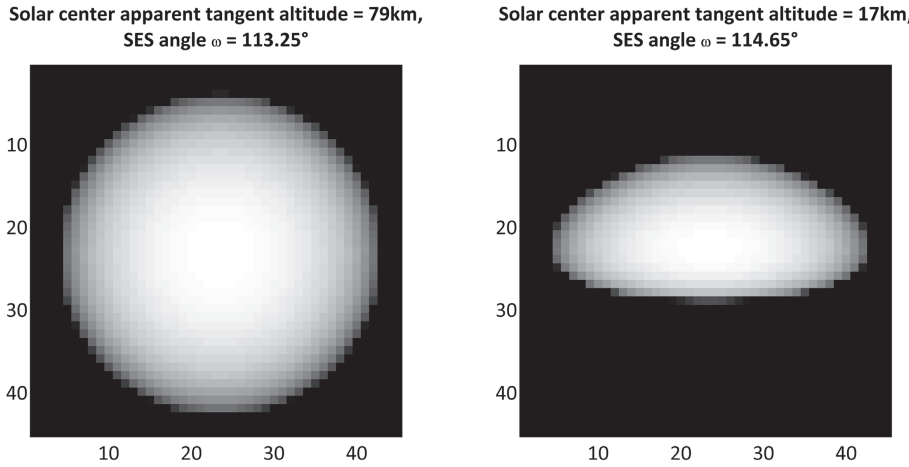

Fig. 2. Simulated pictures of the Sun. Left picture shows a high Sun, right picture shows a low Sun already experiencing strong flattening. Notice the asymmetrical flattening.

AMTD
5, 7535–7565, 2012

Zernike polynomials applied to solar disk flattening

E. Dekemper et al.

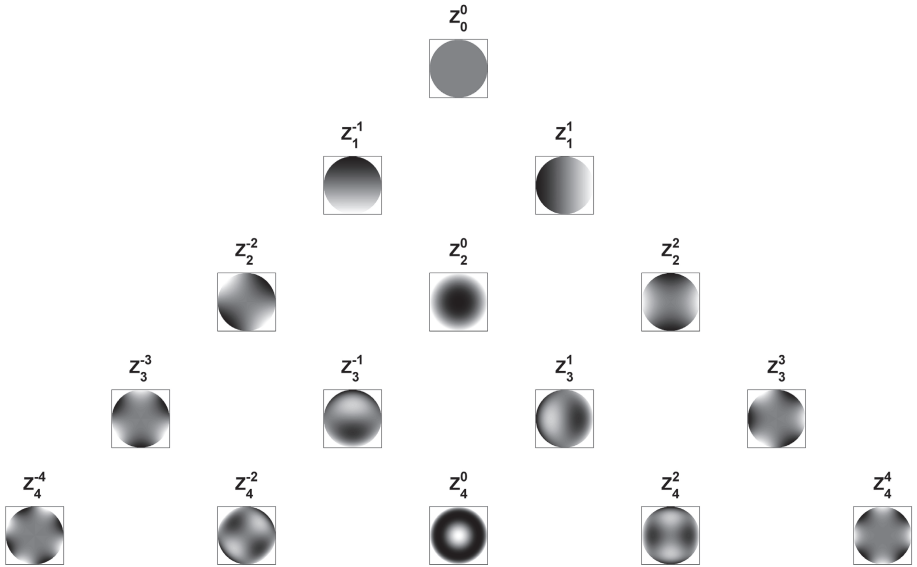

Fig. 3. Zernike polynomials evaluated on the unit disk up to order $n = 4$.

AMTD
5, 7535–7565, 2012

Zernike polynomials applied to solar disk flattening

E. Dekemper et al.

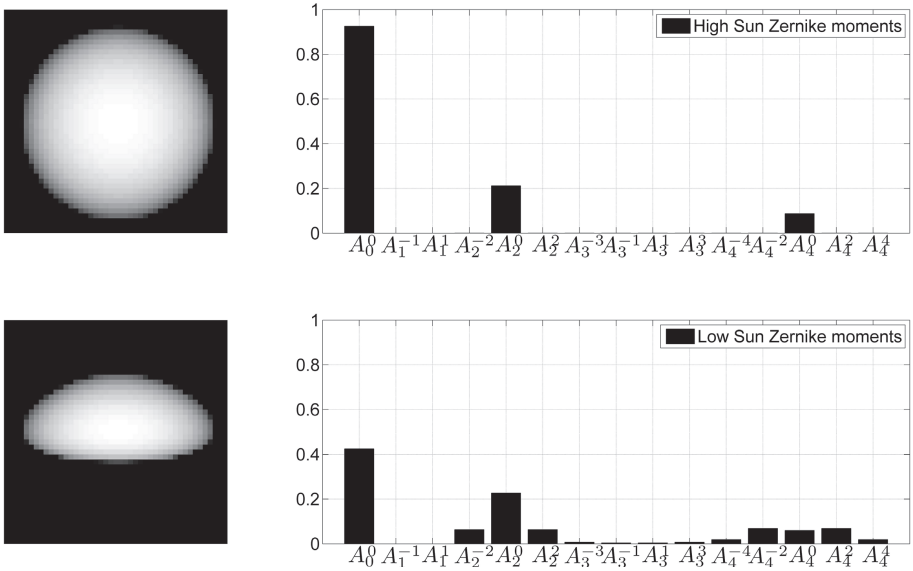

Fig. 4. First 15 Zernike moments computed on a high Sun image and a low Sun image. The moments modulus have been normalized. In the case of the high Sun image, moments with radial features ($m = 0$) are the only ones to play a role in characterizing this unrefracted solar disk. For the low Sun, more moments are needed to account for the asymmetrical flattening.

AMTD
5, 7535–7565, 2012

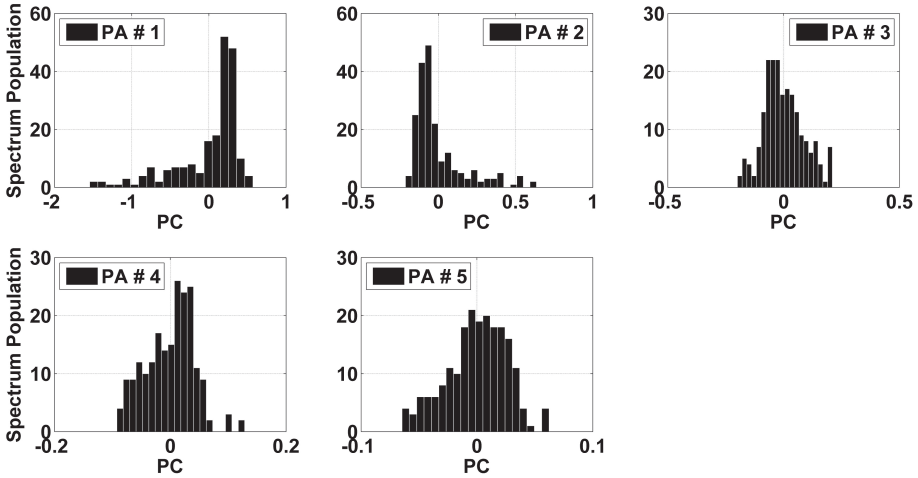

Fig. 5. Distribution of the PCs of the CIRA-86 dataset along the five first principal axes. From these distributions, pivots can be defined in order to generate a training dataset of non-redundant elements.

AMTD
5, 7535–7565, 2012

Zernike polynomials applied to solar disk flattening

E. Dekemper et al.

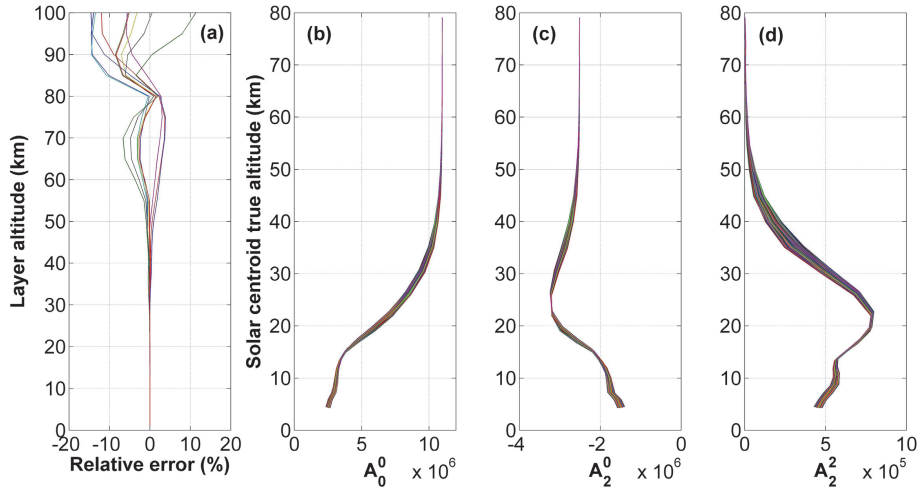

Fig. 6. (a) shows the relative deviation of ten retrieved profiles from the true ones for a retrieval using A_0^0 only. The ten profiles were generated from a combination of random values lying in the range delimited by the PC pivots. **(b)**, **(c)** and **(d)** show the evolution of three Zernike moments with respect to the tangent altitude of the solar disk centroid for the entire training dataset. Noticeable differences between distinct pressure states appear from 60 km and lower.

AMTD
5, 7535–7565, 2012

Zernike polynomials applied to solar disk flattening

E. Dekemper et al.